

Cite this: *Catal. Sci. Technol.*, 2020,
10, 5501

Size dependent oxygen reduction and methanol oxidation reactions: catalytic activities of PtCu octahedral nanocrystals†

Shlomi Polani, *^a Meital Shviro, ^{bc} Victor Shokhen,^a Melina Zysler,^a
Andreas Glösen, ^c Rafal Dunin-Borkowski, ^b
Marcelo Carmo^c and David Zitoun *^a

The synthetic control through colloidal synthesis led to a remarkable increase in platinum mass activity in octahedral nanocrystals with a Pt-rich surface. In this manuscript, we demonstrate that the ratio of surfactant can tune the size of Pt surface enriched PtCu nano-octahedra from 8 to 18 nm with homogeneous size and shape on the carbon support. For the nano-octahedra, the Pt-rich surface has been determined by high-angle annular dark field scanning transmission electron microscopy and energy-dispersive X-ray spectroscopy. The Pt-rich surface exhibits an increasing compressive strain with increasing surface of the {111} facets. With increasing surface, the PtCu nano-octahedra display higher oxygen reduction reaction (ORR) activity, which however leads to higher onset over-potentials in the methanol oxidation reaction (MOR) and CO-stripping. This observed trend for a series of size-selected nano-octahedra demonstrates the benefits of controlling the strained {111} Pt surface for the ORR and MOR activity.

Received 16th April 2020,
Accepted 10th July 2020

DOI: 10.1039/d0cy00772b

rsc.li/catalysis

1 Introduction

Proton-exchange membrane fuel cells (PEMFCs) have been the focus of attention for many years, and the main issue remains the quest for a performant, cost-effective and durable electrocatalyst for the complex oxygen reduction reaction (ORR). The standard catalyst, which is used in relatively high loading in the cathodes of fuel cells, consists of active carbons decorated with *in situ* grown Pt or Pt alloy nanoparticles (NPs). To improve the activity of electrocatalysts for the ORR, the materials-by-design strategy where the design relies on the results obtained on well-defined surfaces and segregation-induced thin layers has been highly successful.¹ Early studies on the kinetics of Pt single-crystal planes for the ORR are found to vary with the crystallographic orientation. Amongst the three low index faces, the activity increases in the order of (100) < (110) = (111).² Studies

conducted on Pt-based extended surfaces show volcano-type behavior on the ORR activity, where the alloying of Pt with 3d-transition metals or lanthanides enhances the ORR activity.^{3–6} These surfaces are highly active due to the formation of segregated Pt-skin and Pt-skeleton strained surfaces with a down-shifted d-band center relative to pure Pt. The electrocatalytic trends established for extended surfaces are useful to provide a fundamental basis to explain the activity pattern of Pt-based nanocatalysts. Controlling the surface structure of Pt and Pt-based NPs has been studied to maximize their catalytic efficiency by selecting the exposed crystal facets and composition for the intended reaction.⁷ Furthermore, dealloying processes where the less noble metal is dissolved allow control over surface composition. Dealloying can be achieved through different means such as annealing, electrochemical or chemical treatment.^{8–16} The Pt-enriched surface layers supported on an alloy core with a smaller lattice parameter display a strain in the shell. Bimetallic NP structures can display Pt-rich surfaces and the atomic spatial distribution is highly dependent on the reaction conditions.^{17–19} Bimetallic Cu@Pt core@shell nanoparticles have been previously prepared and studied for the ORR. They performed better than alloy catalysts and commercial catalysts. This behavior was attributed to the ligand and strain effects of the underlying core metal on the Pt surface layer.^{20–24}

The group of J. K. Nørskov^{25–27} detailed the potential-determining steps (PDS) for the ORR on platinum as the

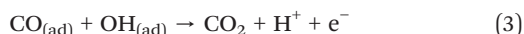
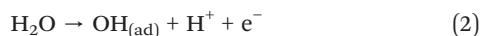
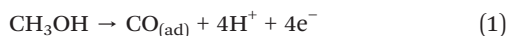
^a Department of Chemistry, Bar-Ilan Institute for Technology and Advanced Materials (BINA), Bar-Ilan University, Ramat Gan, 5290002, Israel.
E-mail: Polani@tu-berlin.de, David.Zitoun@biu.ac.il

^b Ernst Ruska-Centre for Microscopy and Spectroscopy with Electrons and Peter Grünberg Institute, Forschungszentrum Jülich GmbH, 52425 Jülich, Germany

^c Institute of Electrochemical and Climate Research IEK-14, Forschungszentrum Jülich GmbH, 52425 Jülich, Germany

† Electronic supplementary information (ESI) available: Additional TEM data (Fig. S1–S3 and S6) and additional electrochemical measurements (Fig. S4, S5 and S8). See DOI: 10.1039/d0cy00772b

hydrogenation of adsorbed OH and O, caused by $\text{OH}_{(\text{ad})}$ and $\text{O}_{(\text{ad})}$ being too strongly bound to the surface for optimal activity, which can be reached by a catalyst binding $\text{OH}_{(\text{ad})}$ about 0.1 eV weaker than platinum.²⁸ The methanol oxidation reaction (MOR) also involves $\text{OH}_{(\text{ad})}$ as an intermediate species. In general, the indirect path of the complete electro-oxidation of methanol on monometallic surfaces is a three-step process:



A decent MOR catalyst needs to satisfy the following three conditions: (a) actively forms CO from methanol; (b) activates water easily; (c) binds both $\text{CO}_{(\text{ad})}$ and $\text{OH}_{(\text{ad})}$ moderately so CO_2 can be formed. Methanol oxidation is hindered on pure Pt due to methanol adsorption and oxidation on the Pt surface atoms yields $\text{CO}_{(\text{ad})}$, which poisons the catalyst by blocking the active sites.²⁹ The presence of copper may facilitate the adsorption of hydroxyl species from water activation, which subsequently reacts with the CO-groups on the Pt surface atoms to form CO_2 and free active sites. The bifunctionality effect is relevant to bimetallic surfaces such as PtCu alloyed nanoparticles.³⁰ The main effect governing core@shell electrocatalyst activity is the strain.

Using density functional theory (DFT), Tritsaris and Rossmeisl³¹ provided insights into the chemical reactions relevant to the MOR. They treated the MOR catalyst development by correlating the adsorption energies of key MOR intermediates, $\text{OH}_{(\text{ad})}$ and $\text{CO}_{(\text{ad})}$ ($\Delta G_{(\text{CO})}$, $\Delta G_{(\text{OH})}$), to the reaction overpotential. A volcano plot separated into three distinct regions, each corresponding to a different potential-determining step (PDS), was constructed, and the reaction overpotentials were approximated as well. Monometallic platinum surfaces are found in the region where the PDS is eqn (2) due to platinum's poor ability to activate water. A shift toward a more negative $\Delta G_{(\text{OH})}$ value for monometallic platinum will lead to a lower over-potential. In a volcano plot, a low value for the minimum MOR potential does not necessarily correspond to an experimentally measured high activity. The kinetics can be influenced by the size of the surface available for the reaction, especially when a relatively large molecule such as methanol is oxidized. It is well known that the shape of the NPs influences the catalytic properties due to the specific surface atomic arrangement and coordination.^{32,33} Shape-controlled synthesis of Pt-based nanocrystals has been widely studied, leading to the development of multiple strategies to control the shapes of Pt-based nanocrystals with diverse compositions.^{34–37} Strategies have focused on manipulating the exposed facets by employing specific shape-directing agents. CuPt octahedral NPs have been reported in the literature, with shape-directing agents such as CTAB,³⁸ CTAC,³⁹ Γ^- ,⁴⁰ and CO

gas.⁴¹ The effect of different precursor–ligand couples has been investigated⁴¹ and ternary CuPtM (M = Pd and Ni) has been synthesized as well.^{42,43}

Here, we report a highly efficient strategy for a one-pot synthesis of well-defined PtCu octahedral nanocrystals dispersed on carbon in which the size is tunable. PtCu octahedral NPs with size ranging from 8 to 18 nm have been prepared by adjusting the amount of CTAB, while the other synthesis parameters remain unchanged. The successful fabrication of crystal-controlled PtCu octahedral nanocrystals with identical exposed facets and the same compositions provides an ideal case for studying the size effect of {111} facets on ORR and MOR electrocatalysis. We found that all the PtCu octahedra exhibit higher electrocatalytic activities for the ORR and MOR than commercial Pt/C, and the ORR specific activity increases with the particle size; an opposite trend was observed for the MOR onset potentials.

2 Experimental

2.1 Materials

Platinum(II) acetylacetonate ($\text{Pt}(\text{acac})_2$, 97%), nickel(II) acetylacetonate ($\text{Ni}(\text{acac})_2$, 95%), benzoic acid ($\text{C}_6\text{H}_5\text{COOH}$, $\geq 99.5\%$), *N,N*-dimethylformamide (DMF, $\geq 99.9\%$), cetyltrimethylammonium bromide (CTAB, 99%) and Nafion (wt% 5) were all purchased from Sigma-Aldrich. Commercial Pt/C was obtained from Johnson Matthey (JM, 20 wt% Pt). Carbon black (C, Vulcan XC72R carbon) was purchased from Cabot Corporation. All the chemicals were used as received without further purification.

2.2 Synthesis of CuPt/C octahedral NPs

In a typical synthesis of the octahedral PtCu/C catalyst, 10 mg $\text{Pt}(\text{acac})_2$, 6.6 mg $\text{Cu}(\text{acac})_2$, 60 mg benzoic acid, 10 mL carbon black dispersed in DMF (2 mg mL^{-1}) and a CTAB amount corresponding to the desired particle size were added into a vial (20% wt metal loading). After the vial had been capped, the mixture was ultra-sonicated for 15 minutes. The resulting homogeneous mixture was then heated to 160 °C for 12 h before it was allowed to cool down to room temperature. The resulting colloidal products were collected by centrifugation and washed three times with an ethanol/acetone mixture. PtCu/C octahedral catalysts of 8, 10, 14 and 18 nm (vertex to vertex along the $\langle 100 \rangle$ direction) were synthesized by adding 5, 10, 15 and 20 mg of CTAB, respectively. Synthesis of Pt/C was done in the absence of CTAB.

2.3 Morphological, structural, and elemental characterization

The structure of the NPs was investigated using transmission electron microscopy (TEM): JEOL 1400 at 120 kV. The high-angle annular dark-field scanning transmission electron microscopy (HAADF-STEM) micrographs and electron dispersive spectroscopy (EDX) maps were acquired using a monochromatic and double corrected Titan Themis G2 60-

300 (FEI/Thermo Fisher) operated at 300 keV and equipped with a Dual-X detector (Bruker). The quantitative analysis of the EDX maps was done using the Velox software (FEI/Thermo Fisher). Scanning TEM (STEM) was performed at 200 kV on an FEI Titan 80-("ChemiSTEM")⁴⁴ equipped with a C_s-probe corrector (CEOS GmbH) and a high-angle annular dark-field (HAADF) detector operated at 200 kV. A probe semi-angle of 25 mrad and an inner detector collection semi-angle of 88 mrad were used to achieve Z-contrast conditions. EDX compositional maps were obtained using four symmetric large-solid-angle silicon drift detectors. For EDX measurement, an FEI double-tilt holder was used, and the TEM specimen was not tilted. EDX analysis was performed using ESPRIT software (Bruker Company, Berlin, Germany) using the Cu and Pt L peaks. The crystalline phases and crystallinity of the prepared powders were examined by XRD using Cu K α (0.1541 nm) radiation (Bruker Advance D8).

2.4 Electrochemical measurements

A typical three-electrode cell was used to perform the electrochemical measurements. The working electrode was a glassy carbon rotating disk electrode (RDE) (0.196 cm², Pine Instrument). A hydrogen electrode was used as the reference electrode (Gaskatel, HydroFlex) and Pt wire was used as the counter electrode. A catalyst ink was prepared by mixing the as-prepared catalyst CuPt/C powder in ethanol, water, and Nafion (5%) (v/v/v = 8:2:0.01) and sonicated for 45 min in an ice bath. 7.5 microliters of the catalyst ink were cast on the RDE and dried under ambient conditions. The Pt mass was calculated from light elemental analysis in conjunction with EDS elemental analysis for the metallic elemental quantification. The amount of catalyst to target a specific Pt loading was added to a solution of ultrapure water. The loading amount of metal Pt for the PtCu/C octahedral catalysts was $2.4 \pm 0.6 \mu\text{g}_{\text{Pt}}$ ($\sim 12 \pm 3 \mu\text{g}_{\text{Pt}} \text{cm}^{-2}$). For comparison, commercial Pt/C catalyst JM was used as the baseline catalyst with a Pt loading of $10 \mu\text{g}_{\text{Pt}} \text{cm}^{-2}$. Cyclic voltammetry (CV) measurements were conducted in a 0.1 M HClO₄ argon-saturated solution with a potential scan rate of 100 mV s⁻¹. Oxygen reduction reaction (ORR) measurements were conducted in a 0.1 M HClO₄ solution, which was purged with oxygen during the measurement. Linear sweep voltammetry (LSV) was done at a scan rate of 10 mV s⁻¹ and the ORR polarization curves were collected at 400, 625, 900, 1225 and 1600 rpm (only the latest speed is shown). The ECSAs were determined by integrating the hydrogen adsorption charge into the CV. The durability test was performed for 3700 cycles at 900 rpm in oxygen saturated 0.1 M HClO₄ solution from 0.6 V to 1 V vs. RHE at a sweep rate of 50 mV s⁻¹. The CV and LSV were recorded before and after the durability test, at 1600 rpm under Ar and O₂-saturated atmosphere, respectively. For chronoamperometry of the methanol oxidation reaction, an argon-saturated aqueous solution containing 0.1 M methanol and 0.1 M HClO₄ was used. For CO-stripping experiments, CO was adsorbed on the

electrode by holding the potential at 0.05 V (dosing potential), for 60 min in which CO was adsorbed in CO-saturated solution for 25 min followed by 35 min of Ar-purging. Afterward, CV for CO-stripping and CV after CO oxidation from 0.05 V to 1.25 V and back to 0.05 V were conducted. Measurements were conducted in a 0.1 M HClO₄ argon-saturated solution with a potential scan rate of 100 mV s⁻¹.

3 Results and discussion

PtCu octahedral nanocrystals supported on carbon (20% wt metal) with a 1/1 Pt:Cu ratio were prepared using dimethylformamide with benzoic acid and cetyltrimethylammonium bromide (CTAB), which act as capping agents, using a solvothermal method as described in the Experimental section. Tuning the amount of CTAB itself was a facile and robust way to achieve control over size. TEM images (Fig. S1[†]) show the homogeneity of the PtCu octahedral shape and the corresponding narrow particle size distribution (PSD). CuPt octahedral NPs uniformly dispersed on high-surface-area carbon supports with sizes of 8, 10, 14 and 18 nm (vertex-to-vertex along the <100> direction) were prepared by employing 5, 10, 15 and 20 mg of CTAB, respectively, under otherwise constant conditions. In the following, the samples are labeled as PtCu-*S* where *S* indicates the vertex-to-vertex particle size in nm along the <100> direction.

In Fig. S2,[†] the dependency of particle mean size on the amount of CTAB is presented; the linear fit shows a slope of 0.66 nm mg⁻¹ and interception at 4.7 nm corresponding to the size of NPs synthesized without CTAB. The formation of PtCu/C crystalline octahedral NPs is evident from high-angle annular dark-field scanning transmission electron microscopy (HAADF-STEM) images (Fig. 1).

To further explore the HAADF-STEM images, we investigated the particles with STEM-EDX elemental mapping. All these NPs showed a uniform morphology with composition ratio Pt/Cu = 1. The elemental maps of PtCu-8 and PtCu-10 show a platinum-rich surface and copper-rich core (Fig. 2A and B). STEM-EDX line scan analysis was applied, as shown in Fig. S3A and B,[†] and the platinum and copper atomic distributions were studied in octahedral NPs

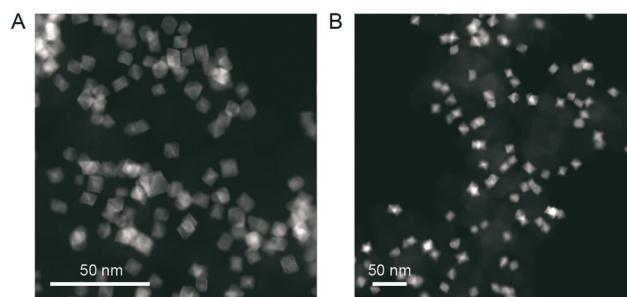


Fig. 1 HAADF-STEM images of (A) CuPt/C octahedral NPs 10 nm (PtCu-10) and (B) 18 nm (PtCu-18).

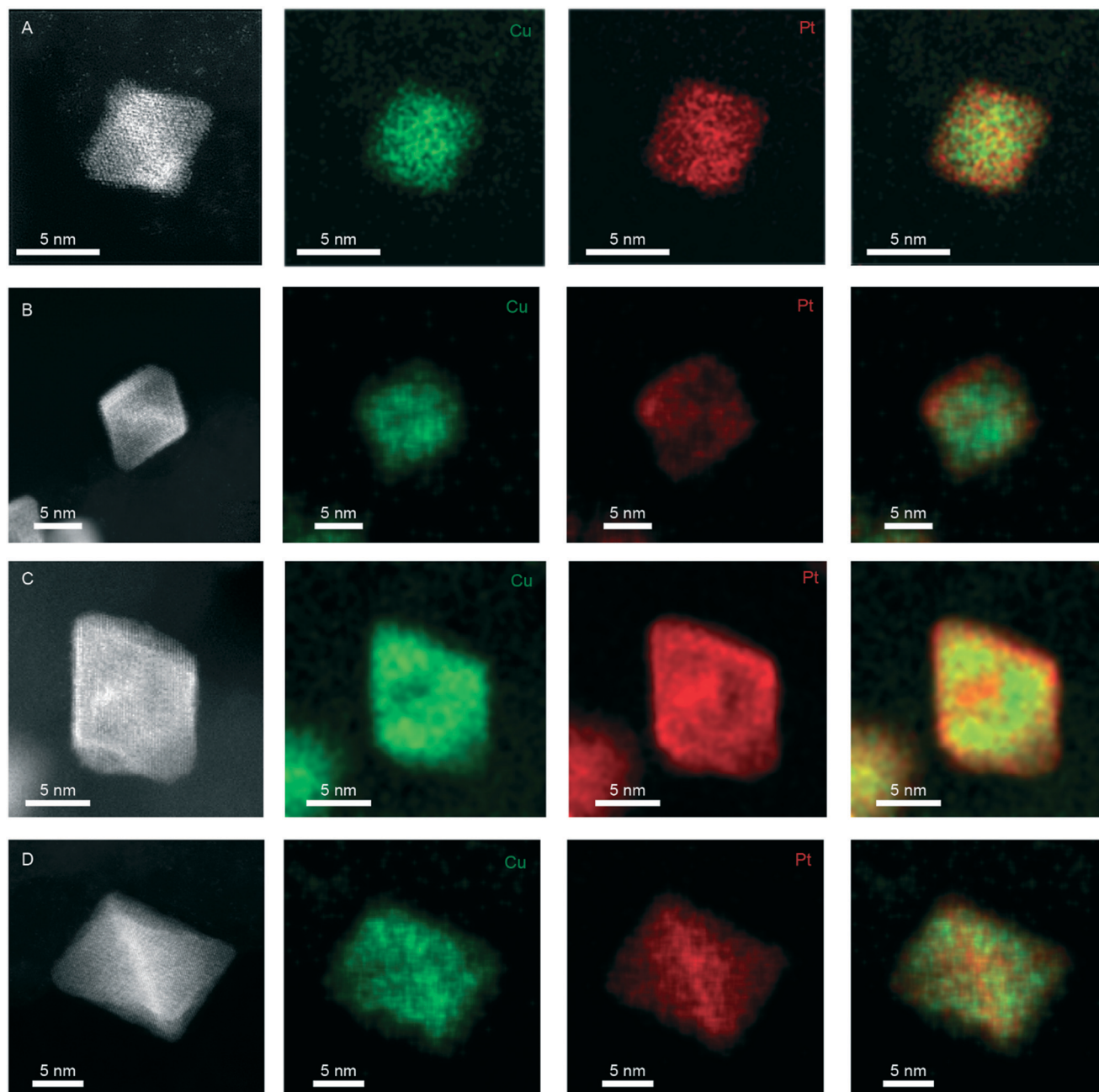


Fig. 2 High resolution HAADF-STEM images and EDX elemental mapping of Cu, Pt and their overlay for PtCu-8, PtCu-10, PtCu-14, and PtCu-18 (panels A–D, respectively).

oriented along the (100) zone axes. Line scans along the (110) direction started and ended at the edges, passing through the central octahedron axis. The relative intensities showed a clear Pt enrichment on the surface compared to the Cu-rich core. From the intensity of the elemental line profiles, platinum and copper segregation occurs close to the nanoparticle edge (Fig. S3A and B†). The elemental segregation observed with the formation of a platinum-rich surface is consistent with the observations reported by Strasser *et al.* on inhomogeneous bimetallic nanoparticles after dealloying.⁸ The relatively lower standard reduction

potential of copper leads to metal etching on the surface of the NPs through galvanic replacement by the Pt^{n+} species and possible oxidative etching in solution. Different nucleation windows of the components and adsorbate induced segregation can lead to surface enrichment as well. In the PtCu system, positive segregation energy should drive Cu to the surface ($\Delta E_{(\text{Cu})\text{Pt}} = 0.41 \text{ eV}$).⁴⁵ However, as observed for most of the Pt-based bimetallic particles, the system seems to be driven by the presence of surface ligands, namely benzoic acid, which preferentially coordinate and leach out the Cu surface atoms.

Upon the increase of CTAB, the PtCu system still shows a Pt-rich surface with a slightly different atomic distribution. PtCu-14 and PtCu-18 display Pt-rich edges, as observed from EDX mapping (Fig. 2C and D). STEM-EDX

line analysis was also applied, as shown in Fig. S3C and D,[†] and the platinum and copper atomic distributions were studied in octahedral NPs oriented along the (100) zone axes.

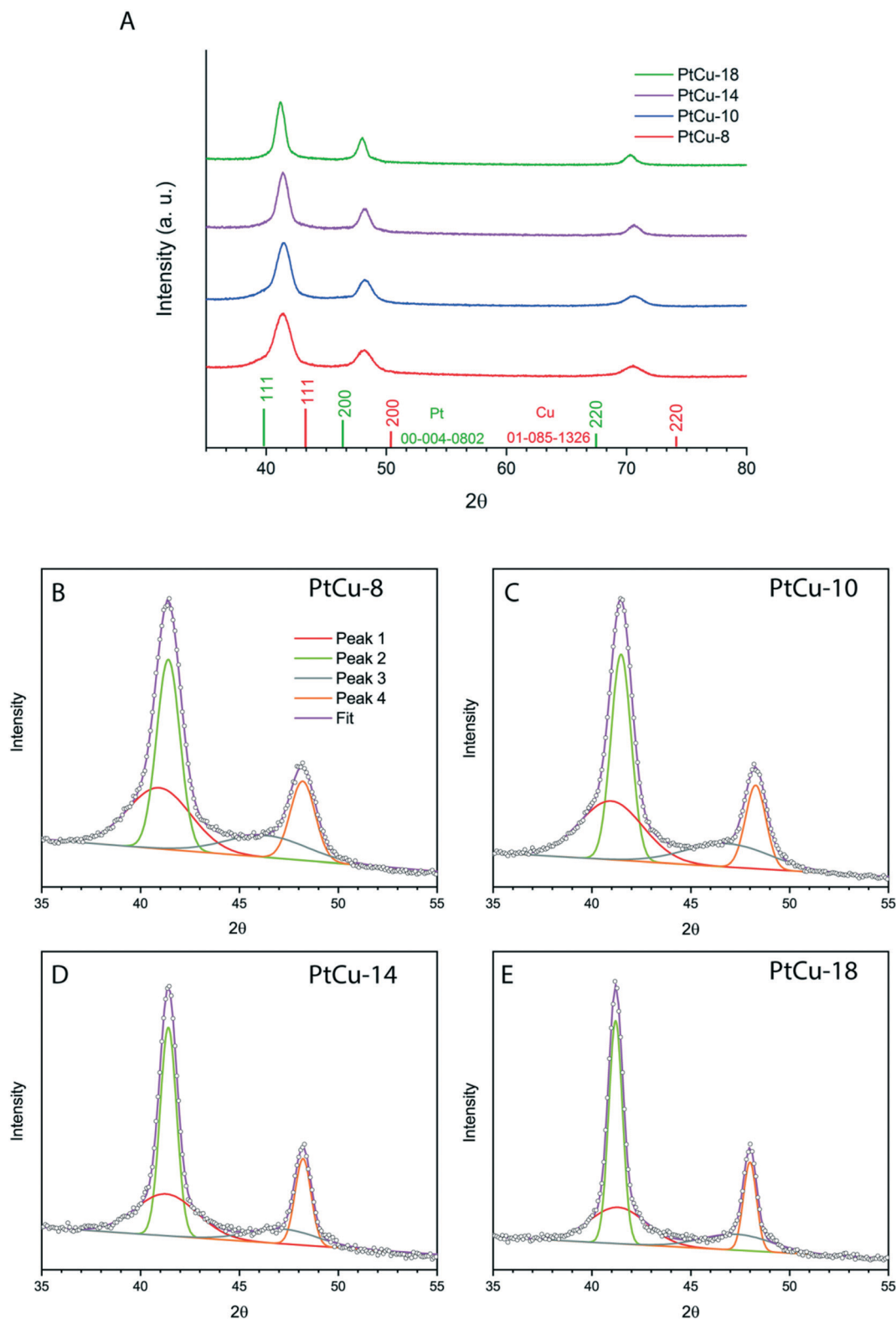


Fig. 3 XRD patterns of PtCu octahedral NPs (A); deconvolution of the (111) and (200) Bragg reflections for PtCu-8 to Pt-Cu-18 (B–E, respectively).

The XRD patterns indicate that the PtCu NPs are single-crystal face-centered cubic (FCC) structures with a $\{111\}$ interplane distance in between that of pure Pt (2.26 Å) and Cu (2.09 Å). The XRD patterns of the NPs synthesized with an increasing amount of CTAB also show a sharpening of the peaks, which is consistent with the increase in particle size (Fig. 3A). We observe a shoulder of the (111) peak at $2\theta \sim 42^\circ$ (named as peak 1). This asymmetry is due to a broader secondary peak at the lower 2θ , arising from the Pt-rich surface. The asymmetry is more visible on the PtCu-8 sample (Fig. 3B) and diminishes as the particle size increases.

Fig. 3B–E show the fitting of typical profiles of the different particle sizes; two Gaussian functions fit well the (111) and (200) reflections of all the samples. For the (111) reflection, the two peaks are identified as peak 1, which corresponds to the Pt-rich shell, and peak 2, which correspond to the Cu-rich core. For the (200) reflection, the two peaks are identified as peak 3 and peak 4. Peak 1 center is shifted to smaller unit cells from PtCu-8 to PtCu-18, which suggests that the Pt-rich shell in PtCu-8 displays lattice parameters closer to bulk Pt. Eqn (S1) in the ESI† was used to calculate the strain imposed on the Pt surface. Peak 1 corresponds to a_{shell} , and a_{core} corresponds to the bulk lattice parameter of Pt(111). The a_{shell} parameters were taken from the deconvoluted XRD band of peak 1. For PtCu-8, PtCu-10, PtCu-14 and PtCu-18, the corresponding lattice parameters for peak 1 are 3.75 nm, 3.72 nm, 3.7 nm, and 3.69 nm, respectively. For PtCu-8 and PtCu-10 with a clear Cu-core and Pt-shell structure, it implies that the Pt-rich shell exhibits a compressive strain of 1.4% and 2.2%, respectively. For PtCu-14 and PtCu-18, where the surface is mixed Pt edges and Cu facets, the compressive strain reaches 3%. The XRD results

are in agreement with the EDX results and suggest the interplay between particle size and the number of Pt layers on the surface in our case study. Comparable asymmetry has been described for dealloyed PtCu₃ films by Yang *et al.*¹¹ and for octahedral MPt (M = Cu or Ni) by LaGrow *et al.*⁴¹

We performed precisely the same reaction but, in the absence of CTAB. The PtCu octahedral NPs could not be formed, only spherical NPs with the smallest particle size of 4.6 ± 0.6 nm and a pure Pt composition according to the EDX results (Fig. 4). The XRD pattern shows the presence of a Cu pure phase with much sharper Bragg reflections than those of the Pt phase (Fig. 4A), which is consistent with the slow formation of large Cu nanoparticles that could not be observed by TEM. To further explore the role of CTAB in the synthesis, we reacted Cu(acac)₂ alone into two vials, the first contains only DMF while the second contains DMF and CTAB. After heating the vials to 160 °C, we observe the formation of Cu nanoparticles after half an hour in the absence of CTAB and 4 hours in the presence of CTAB. The slow kinetics in the presence of CTAB explain the finding that the CTAB concentration directly correlates to the NP size since the slow reaction kinetics yield fewer nucleation centers and, therefore, larger particles. Moreover, only the presence of CTAB can direct the formation of uniform and monodisperse octahedral nanocrystals by slowing down the reaction kinetics. At the same time, unshaped particles are formed in its absence (Fig. 4B). These results suggest a kinetic role played by CTAB, which can change the reduction rate and nucleation window of Cu complexes by forming micelles⁴⁶ and subsequently acts as a capping agent to stabilize the Pt{111} facets.⁴⁷ The octahedral shape itself can be explained by the stabilization of the $\{111\}$

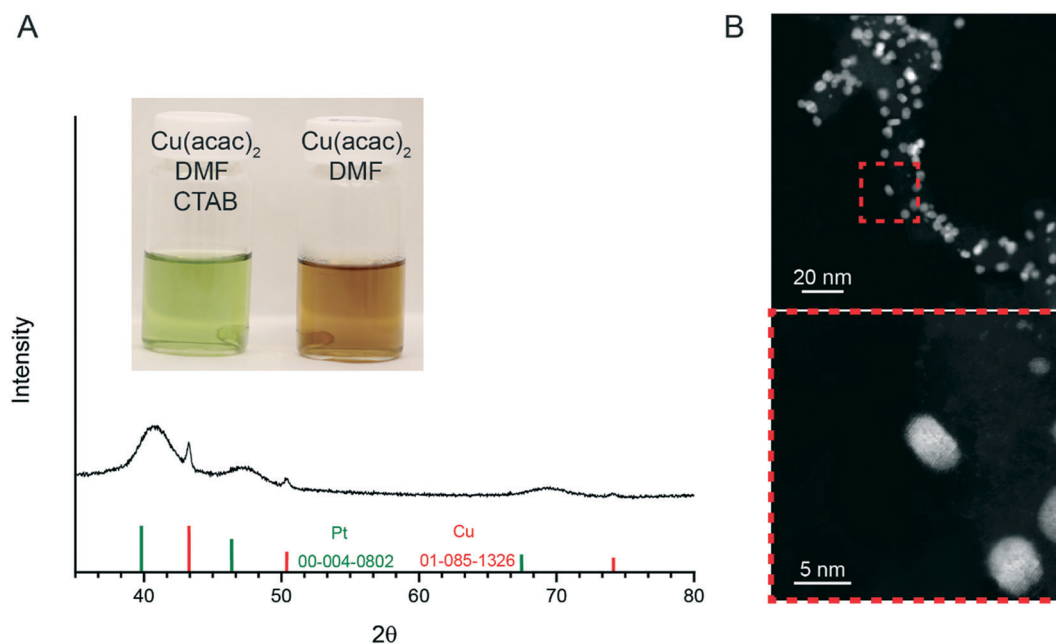


Fig. 4 (A) XRD of the synthesis without CTAB and photographs of the vials after reaction (inset). (B) HAADF-STEM images of the Pt nanoparticles obtained without CTAB.

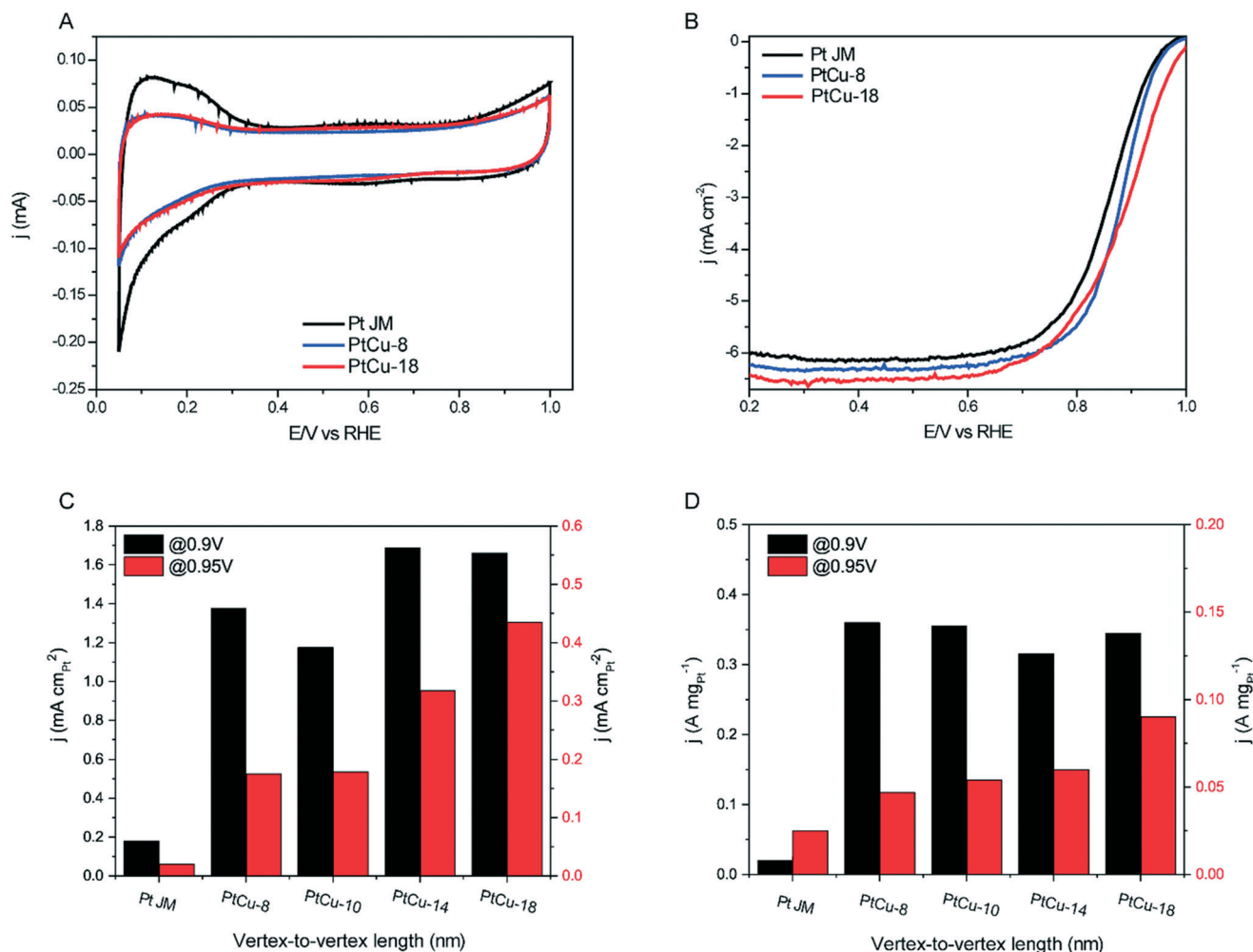


Fig. 5 (A) CVs recorded at room temperature in an Ar-saturated 0.1 M HClO₄ solution with a sweep rate of 100 mV s⁻¹. (B) ORR polarization curves recorded at room temperature in an O₂-saturated 0.1 M HClO₄ aqueous solution with a sweep rate of 10 mV s⁻¹ and a rotation rate of 1600 rpm, normalized over the geometric surface area of the working electrode. (C & D) Specific and mass activity, respectively, for the ORR at 0.9 and 0.95 V for all the catalysts.

facets of Pt or Pt-rich surfaces in the presence of a bromide ligand.^{36,48,49}

For the electrocatalytic study, we recorded cyclic voltammetry (CV) at 298 K in 0.1 M HClO₄ solution at a sweep rate of 100 mV s⁻¹ (Fig. 5A and S4A†). The electrochemical surface areas (ECSAs) were calculated from the H_{UPD} and reach the values of 26.82, 30.23, 18.69 and 20.75 m² g⁻¹ for PtCu-8, CuPt-10, PtCu-14, and PtCu-18, respectively, and 116.2 m² g⁻¹ for the standard catalyst (Pt/C 20% from Johnson-Matthey, named Pt JM in the following). Fig. 5B shows the ORR polarization curves of PtCu-8, PtCu-18, and Pt JM obtained in an oxygen-saturated 0.1 M HClO₄ solution at a sweep rate of 10 mV s⁻¹ and at a rotation rate of 1600 rpm (for PtCu-10 and PtCu-14, see Fig. S4B†). From the polarization curves, the calculated kinetic current density at 0.9 V and 0.95 V were normalized over the Pt loading weight and ECSA to give the mass activity and specific activity, respectively (Fig. 5C and D). We found that the catalytic specific and mass activities of all the PtCu octahedral NPs

are greater than those of Pt JM. At 0.9 V, PtCu-8 showed a specific activity of 1.38 mA cm_{Pt}⁻² and a mass activity of 0.34 mA mg_{Pt}⁻¹, a 6.9 times higher specific activity and 2-fold mass activity enhancement compared to Pt JM (0.2 mA cm_{Pt}⁻² and 0.17 mA mg_{Pt}⁻¹). With increasing size, the mass activity remains constant while the specific activity slightly increases to 1.58 mA cm⁻² for the PtCu-18 octahedra.

The main result concerns the increasing trend in ORR onset potential observed with increasing vertex-to-vertex length of the octahedra. The current at 0.9 V is in the mixed control region. Nevertheless, it was not possible to further decrease the Pt loading on the electrode while obtaining a homogeneous film. Therefore, we also report the activities at 0.95 V, which is a common practice for recent high activity catalysts.^{50–52} The specific activities at 0.95 V demonstrate the activity enhancement trends with size. PtCu-18 showed a specific activity of 0.44 mA cm_{Pt}⁻² and a mass activity of 0.090 mA mg_{Pt}⁻¹. We found that the specific activity of PtCu-18 is 2.5 times higher than that of PtCu-8 and reveals the

global trend of increasing specific activity for extended {111} facets. Compared to previously reported specific activities, CuPt-8 shows the same activity as Pt₃Cu octahedral NPs with similar size reported by Sun *et al.*³⁸ and Cu@Pt strained NPs.^{8,53}

The size and shape control of PtCu octahedra gave us a chance to observe the influence of the size on the atomic distribution of Cu and Pt, and subsequently on the ORR activity. First, all the octahedra display only {111} facets with a Pt-rich surface for all the particle sizes of the study. Second, the copper core determines the compressive strain on the Pt surface. As the particle size grows, the Pt surface displays an increasing compressive strain up to 3% for PtCu-18. Indeed, in the case of a few layers of the Pt surface, the compressive-strain effects have been shown to be responsible for the high activity of the NPs and we can exclude the role of the vicinity of a second metal (the so-called ligand effect) due to the limited range of this effect.⁵⁴ Qualitatively, the ORR activity scales with the strain of the Pt surface. The highest ORR activity was measured on the 3% strained Pt surface (PtCu-18). For a smaller size, like PtCu-10, the measured strained is only 1.4%, which could explain the lower ORR activity. The thickness of the Pt layer can be estimated from the line scan, together with the HAADF-STEM image. The Pt surface consists of a few atomic layers for PtCu-10. These findings quantitatively match the DFT calculations predicting the relationship between the layer thickness, the strain, and the oxygen binding energy (1.4% strain for 4 atomic Pt layers).⁹

The durability of the ORR electrocatalysts was tested following a DOE procedure, as reported in the Experimental section. We report the results on the most active catalyst: PtCu-18. Fig. S5A† shows the CV before and after the durability test; the H-UPD region slightly decreases after the durability test, and the electrochemical surface area was reduced from 25 m² g_{Pt}⁻¹ to 22 m² g_{Pt}⁻¹. Moreover, the

current densities at 0.9 V and 0.95 decrease by around 1 mA cm⁻² and 0.5 mA cm⁻², respectively. The limiting current was reduced by slightly less than 1 mA cm⁻² after the durability test (Fig. S5B†). These changes lead to a decrease in the kinetic current density by a factor of two. One of the most crucial points in the design of complex particles, like the octahedral PtCu particles of this study, is whether the particle shape can sustain the electrochemical cycling. Therefore, following the durability test, we collected the electrocatalysts from the working electrode and drop-cast them on a TEM grid, including the ionomer used to prepare the catalyst ink, which can explain the low quality of the images (Fig. S6A and B†). Nevertheless, the TEM images show that the distribution, morphology, and size of the octahedral NPs were kept intact during the stability test. Furthermore, Fig. S6C and D† show the TEM micrographs of the PtCu-18 octahedral NPs collected from the working electrode after the CO-stripping test. The octahedral electrocatalysts retain their octahedra original shape, and no major agglomeration can be seen.

We evaluated the electrocatalytic activities of PtCu octahedral NPs for the MOR. The forward peak potential of the 8 nm PtCu octahedral NPs (0.84 V) was lower than that of the 18 nm PtCu octahedral NPs (0.87 V) and approximately the same as that of Pt/C JM (0.83 V) (Fig. 6A). The forward peak potentials of PtCu-10 and PtCu-14 are 0.86 V and 0.87 V, respectively (Fig. S7A†). The forward peak current densities of the different catalysts were normalized over the Pt loading weights and ECSAs to give the mass activities and current densities, respectively. The mass and specific activities of all the catalysts for the MOR are summarized in Fig. 6B in which the 18 nm PtCu octahedral NPs exhibit the highest mass activity and specific activity. The mass activity of 8 and 18 nm CuPt/C octahedral NPs is measured to be 495 and 521 mA mg_{Pt}⁻¹, respectively, which is on average 4.42 times higher

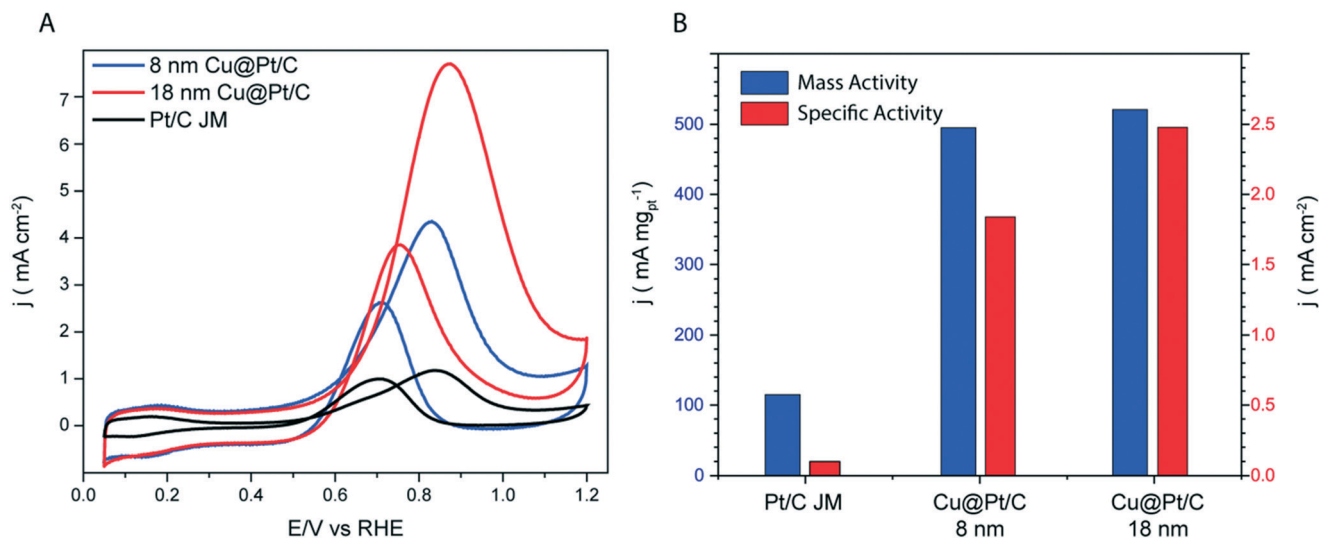


Fig. 6 (A) CVs recorded at room temperature in the mixture of 0.1 M HClO₄ and 0.1 M CH₃OH solution with a sweep rate of 100 mV s⁻¹ normalized over the geometric surface area of the working electrode. (B) Specific and mass activities of the electrocatalysts.

than that of Pt/C. Similarly, the 18 nm PtCu octahedral NPs exhibit up to 1.35 and 24.8 times higher specific activity ($2.48 \text{ mA cm}_{\text{Pt}}^{-2}$) than the 8 nm PtCu octahedral NPs and Pt/C JM, respectively. The specific activities of the 10 and 14 nm PtCu octahedral NPs are 1.89 and $2.1 \text{ mA cm}_{\text{Pt}}^{-2}$, respectively, and fall in the range between the results for the 8 to 18 nm PtCu octahedral NPs. The mass activity of the 10 and 14 nm PtCu octahedral NPs is 560 and $391 \text{ mA mg}_{\text{Pt}}^{-1}$, respectively (Fig. S7B†).

We correlate the current density at the forward peak potential to the size of the NPs, where larger catalytic surfaces will promote the kinetics of the reaction compared with smaller surfaces especially for relatively large fuels like methanol (relative to dihydrogen). Yet, the forward peak potential for the oxidation of methanol demonstrates an opposite trend. The methanol oxidation overpotential for the smallest (PtCu-8) catalyst is the lowest overpotential, correlating to the decrease of the strain with the decrease in NP size.

To gain insight on the $\text{CO}_{(\text{ad})}$ adsorption energy, we performed stripping voltammetry of $\text{CO}_{(\text{ad})}$ on PtCu octahedra with different sizes and strained surfaces. Fig. S8† shows the stripping voltammetry curves of $\text{CO}_{(\text{ad})}$ on PtCu octahedral NPs in 0.1 M HClO_4 solution, onto which the CVs are superimposed in Ar-saturated solutions. The peak potential correlates to the NP size, and to the strain of the PtCu octahedral NPs. PtCu-18, which is the most strained (3%), shows the highest over-potential to oxidase the adsorbed CO at 0.8 V, and PtCu-8 with the lowest strain (1.4%) shows an over-potential of 0.69 V (for PtCu-10 and PtCu-14, the over-potentials are 0.71 V and 0.79 V, respectively).⁵⁵ The interpretation of CO-stripping voltammetry on a Pt (111) single crystal in sulfuric and perchloric acid has been previously discussed in the literature. Marković *et al.*⁵⁶ reported the oxidation of $\text{CO}_{(\text{ad})}$ on a Pt (111) single crystal. Above 0.6 V, the stripping voltammetry is characterized by two sharp peaks, a minor peak at *ca.* 0.68 V and a major peak at $\approx 0.75 \text{ V}$, which was assigned to strong binding $\text{CO}_{(\text{ad})}$. The stripping voltammetry curve at $E > 0.6 \text{ V}$ is determined by the gentle balance concerning the surface nature of the $\text{CO}_{(\text{ad})}$ layer and the formation of platinum bare sites for adsorption of OH. López-Cudero *et al.*⁵⁷ studied the effect of intentionally created surface defects on the Pt (111) single crystal electrode, and showed that surface defects on the Pt (111) electrode result in a slight negative shift of the main peak potential from the Pt “defect” electrode. They proposed that the process in the pre-peak corresponds to the oxidation of adsorbed CO by the reaction with oxygenated species, which adsorbed at steps and defect sites. The process at the pre-peak corresponds to the oxidation of $\text{CO}_{(\text{ad})}$ by the reaction with $\text{OH}_{(\text{ad})}$ nucleating at steps, the main peak appearing when nucleation of oxygenated species at the terraces occurs.⁵⁷ The bifunctionality effect is also relevant to monometallic surfaces that comprise steps and terraces, a depiction closer to the real morphology of catalytic nanoparticles. A stepped surface can serve as a model for the

low-coordinated surface atoms, in our case study the edges and apexes of the octahedral NPs at which water activation occurs. Meanwhile, $\text{CO}_{(\text{ad})}$ is formed on the terrace, and diffuses to steps and defects during the oxidation of the CO ad-layer in the pre-peak.^{31,57} The trend with the electrocatalyst size can be explain by the ratio of facets to edges and apexes, where the smaller catalysts have a lower ratio and relatively more $\text{OH}_{(\text{ad})}$ available. However, in the ORR, a higher surface atom coordination number for larger octahedra should lead to higher activities.^{58,59} Nevertheless, the results acquired from bulk materials are not always successfully connected to the findings obtained from NPs.⁶⁰ A different interpretation correlates the facets exposed at surfaces of preferentially oriented Pt NPs and nanostructured poly-oriented Pt surfaces that are mesoscopic in size, as suggested by the work of Urchaga *et al.*,⁶¹ where in the case of platinum spherical NPs, the surface exposed is mainly the (100) facets, which show the CO-stripping peak at higher potential than the (111) facets typically exposed by octahedral NPs. Both interpretations can explain the potential at which Pt/C JM oxidizes $\text{CO}_{(\text{ad})}$ compared to the PtCu octahedral NPs. The Pt/C spherical NPs enclosed by the (100) facets do not have edges and apexes for water activation and OH adsorption, compared to PtCu octahedral NPs, which are enclosed by the (111) facets and possess distinct edges and apexes for water activation and OH adsorption. Moreover, the bi-functionality effect of PtRu and PtNi for the MOR, where Ru or Ni ad-atoms adsorb OH at a lower potential, and then $\text{OH}_{(\text{ad})}$ reacts on the surface with $\text{CO}_{(\text{ad})}$ to release the active sites, supports our hypothesis.^{62–64} The strain effect plays a role in the ORR by decreasing the $\Delta G_{(\text{OH})}$ binding energy on strained platinum relative to bulk platinum, which leads to lower over-potential. In CO-stripping and MOR, the compressive strain effect leads to higher over-potential due to the role of $\text{OH}_{(\text{ad})}$ in the surface oxidation reaction with $\text{CO}_{(\text{ad})}$ to produce CO_2 and active sites.

4 Conclusion

The ability to control the size and shape of PtCu octahedra through the simple addition of a non-binding surfactant offers an excellent model to observe the trend in the structure–activity relationship. Indeed, we could attribute the increase of the ORR activity, the low MOR over-potential and CO-stripping potential to the size and atomic distribution of the electrocatalysts. The present work suggests a synthetic approach for controlling the size of the active facet and thus to improve the electrocatalytic performance of ORR and MOR electrocatalysts. The addition of CTAB surfactant in a single step colloidal synthesis of carbon supported copper–platinum nanocrystals promotes the formation of nano-octahedra. The addition of surfactant leads to the linear increase of the octahedral size from 8 to 18 nm with high homogeneity in size and shape. HAADF-STEM combined with EDX demonstrates the presence of a Pt-rich surface on a Cu core which results in compressive strain on the Pt layers. The

increasing ORR specific activity observed with size seems to originate from the high compressive stress. Both MOR and CO-stripping oxidation peaks are correlated to the electrocatalyst size and thus the strain imposed on the platinum surface atoms. After a stability test, the nanocrystals remain octahedral without apparent changes.

Author contributions

The manuscript was written through the contributions of all the authors. All the authors have given approval to the final version of the manuscript.

Conflicts of interest

The authors declare no competing financial interests.

Acknowledgements

This work is supported by the Planning & Budgeting Committee of the Council of High Education and the Prime Minister Office of Israel, in the framework of the INREP project.

References

- 1 V. R. Stamenkovic, D. Strmcnik, P. P. Lopes and N. M. Markovic, Energy and fuels from electrochemical interfaces, *Nat. Mater.*, 2016, **16**, 57–69.
- 2 N. Markovic, Kinetics of Oxygen Reduction on Pt(hkl) Electrodes: Implications for the Crystallite Size Effect with Supported Pt Electrocatalysts, *J. Electrochem. Soc.*, 1997, **144**, 1591.
- 3 V. R. Stamenkovic, *et al.* Trends in electrocatalysis on extended and nanoscale Pt-bimetallic alloy surfaces, *Nat. Mater.*, 2007, **6**, 241–247.
- 4 V. Stamenkovic, *et al.* Changing the Activity of Electrocatalysts for Oxygen Reduction by Tuning the Surface Electronic Structure, *Angew. Chem., Int. Ed.*, 2006, **45**, 2897–2901.
- 5 N. Lindahl, *et al.* High Specific and Mass Activity for the Oxygen Reduction Reaction for Thin Film Catalysts of Sputtered Pt₃Y, *Adv. Mater. Interfaces*, 2017, **4**, 1–9.
- 6 M. Escudero-Escribano, *et al.* Tuning the activity of Pt alloy electrocatalysts by means of the lanthanide contraction, *Science*, 2016, **352**, 73–76.
- 7 P. Strasser, Catalysts by Platonic design, *Science*, 2015, **349**, 379–380.
- 8 P. Strasser, *et al.* Lattice-strain control of the activity in dealloyed core-shell fuel cell catalysts, *Nat. Chem.*, 2010, **2**, 454–460.
- 9 R. Srivastava, P. Mani, N. Hahn and P. Strasser, Efficient oxygen reduction fuel cell electrocatalysis on voltammetrically dealloyed Pt-Cu-Co nanoparticles, *Angew. Chem., Int. Ed.*, 2007, **46**, 8988–8991.
- 10 P. Mani, R. Srivastava and P. Strasser, Dealloyed Pt-Cu core-shell nanoparticle electrocatalysts for use in PEM fuel cell cathodes, *J. Phys. Chem. C*, 2008, **112**, 2770–2778.
- 11 R. Yang, J. Leisch, P. Strasser and M. F. Toney, Structure of dealloyed PtCu₃ thin films and catalytic activity for oxygen reduction, *Chem. Mater.*, 2010, **22**, 4712–4720.
- 12 P. Mani, R. Srivastava and P. Strasser, Dealloyed binary PtM₃ (M=Cu, Co, Ni) and ternary PtNi₃M (M=Cu, Co, Fe, Cr) electrocatalysts for the oxygen reduction reaction: Performance in polymer electrolyte membrane fuel cells, *J. Power Sources*, 2011, **196**, 666–673.
- 13 M. Oezaslan, F. Hasché and P. Strasser, PtCu₃, PtCu and Pt₃Cu Alloy Nanoparticle Electrocatalysts for Oxygen Reduction Reaction in Alkaline and Acidic Media, *J. Electrochem. Soc.*, 2012, **159**, B444.
- 14 E. J. Coleman, M. H. Chowdhury and A. C. Co, Insights into the oxygen reduction reaction activity of Pt/C and PtCu/C catalysts, *ACS Catal.*, 2015, **5**, 1245–1253.
- 15 M. Li, *et al.* Ultrafine jagged platinum nanowires enable ultrahigh mass activity for the oxygen reduction reaction, *Science*, 2016, **354**, 1414–1419.
- 16 D. Wang, *et al.* Tuning Oxygen Reduction Reaction Activity via Controllable Dealloying: A Model Study of Ordered Cu₃Pt/C Intermetallic Nanocatalysts | EFRC Community Website, *Nano Lett.*, 2012, **12**, 5230.
- 17 C. Cui, L. Gan, M. Heggen, S. Rudi and P. Strasser, Compositional segregation in shaped Pt alloy nanoparticles and their structural behaviour during electrocatalysis, *Nat. Mater.*, 2013, **12**, 765–771.
- 18 L. Gan, *et al.* Element-specific anisotropic growth of shaped platinum alloy nanocrystals, *Science*, 2014, **346**, 1502–1506.
- 19 N. Ortiz, R. G. Weiner and S. E. Skrabalak, Ligand-controlled Co-reduction versus electroless co-deposition: Synthesis of nanodendrites with spatially defined bimetallic distributions, *ACS Nano*, 2014, **8**, 12461–12467.
- 20 R. Yang, J. Leisch, P. Strasser and M. F. Toney, Structure of dealloyed PtCu₃ thin films and catalytic activity for oxygen reduction, *Chem. Mater.*, 2010, **22**, 4712–4720.
- 21 P. Strasser, *et al.* Lattice-strain control of the activity in dealloyed core-shell fuel cell catalysts, *Nat. Chem.*, 2010, **2**, 454–460.
- 22 E. J. Coleman, M. H. Chowdhury and A. C. Co, Insights into the oxygen reduction reaction activity of Pt/C and PtCu/C catalysts, *ACS Catal.*, 2015, **5**, 1245–1253.
- 23 N. Hodnik, *et al.* Effect of ordering of PtCu₃ nanoparticle structure on the activity and stability for the oxygen reduction reaction, *Phys. Chem. Chem. Phys.*, 2014, **16**, 13610–13615.
- 24 M. Bele, *et al.* A highly active PtCu₃ intermetallic core-shell, multilayered Pt-skin, carbon embedded electrocatalyst produced by a scale-up sol-gel synthesis, *Chem. Commun.*, 2014, **50**, 13124–13126.
- 25 J. K. Nørskov, *et al.*, Origin of the overpotential for oxygen reduction at a fuel-cell cathode, *J. Phys. Chem. B*, 2004, **108**, 17886–17892.
- 26 G. S. Karlberg, J. Rossmeisl and J. K. Nørskov, Estimations of electric field effects on the oxygen reduction reaction based on the density functional theory, *Phys. Chem. Chem. Phys.*, 2007, **9**, 5158–5161.

- 27 A. E. Russell, Faraday discussions: Preface, *Faraday Discuss.*, 2008, **140**, 9–10.
- 28 I. E. L. Stephens, A. S. Bondarenko, U. Grønbjerg, J. Rossmeisl and I. Chorkendorff, Understanding the electrocatalysis of oxygen reduction on platinum and its alloys, *Energy Environ. Sci.*, 2012, **5**, 6744–6762.
- 29 M. J. Lee, *et al.*, Understanding the Bifunctional Effect for Removal of CO Poisoning: Blend of a Platinum Nanocatalyst and Hydrous Ruthenium Oxide as a Model System, *ACS Catal.*, 2016, **6**, 2398–2407.
- 30 C. Li, *et al.*, Composition-driven shape evolution to Cu-rich PtCu octahedral alloy nanocrystals as superior bifunctional catalysts for methanol oxidation and oxygen reduction reaction, *Nanoscale*, 2018, **10**, 4670–4674.
- 31 G. A. Tritsarlis and J. Rossmeisl, Methanol oxidation on model elemental and bimetallic transition metal surfaces, *J. Phys. Chem. C*, 2012, **116**, 11980–11986.
- 32 N. Tian, Z. Y. Zhou and S. G. Sun, Platinum metal catalysts of high-index surfaces: from single-crystal planes to electrochemically shape-controlled nanoparticles, *J. Phys. Chem. C*, 2008, **112**, 19801–19817.
- 33 Y. Kang, P. Yang, N. M. Markovic and V. R. Stamenkovic, Shaping electrocatalysis through tailored nanomaterials, *Nano Today*, 2016, **11**, 587–600.
- 34 N. S. Porter, H. Wu, Z. Quan and J. Fang, Shape-control and electrocatalytic activity-enhancement of Pt-based bimetallic nanocrystals, *Acc. Chem. Res.*, 2013, **46**, 1867–1877.
- 35 J. Wu and H. Yang, Platinum-Based Oxygen Reduction Electrocatalysts, *Acc. Chem. Res.*, 2013, **46**(8), 1848–1857.
- 36 J. Wang, *et al.*, Recent advances in Pt-based octahedral nanocrystals as high performance fuel cell catalysts, *J. Mater. Chem. A*, 2016, **4**, 11559–11581.
- 37 M. Bele, *et al.*, A highly active PtCu₃ intermetallic core-shell, multilayered Pt-skin, carbon embedded electrocatalyst produced by a scale-up sol-gel synthesis, *Chem. Commun.*, 2014, **50**, 13124–13126.
- 38 X. Sun, K. Jiang, N. Zhang, S. Guo and X. Huang, Crystalline Control of {111} Bounded Pt₃Cu Nanocrystals: Multiply-Twinned Pt₃Cu Icosahedra with Enhanced Electrocatalytic Properties, *ACS Nano*, 2015, **9**, 7634–7640.
- 39 Y. Jia, *et al.*, Composition-tunable synthesis of Pt–Cu octahedral alloy nanocrystals from PtCu to PtCu₃ via underpotential-deposition-like process and their electrocatalytic properties, *RSC Adv.*, 2015, **5**, 18153–18158.
- 40 B. A. Lu, *et al.*, Octahedral PtCu alloy nanocrystals with high performance for oxygen reduction reaction and their enhanced stability by trace Au, *Nano Energy*, 2017, **33**, 65–71.
- 41 A. P. LaGrow, K. R. Knudsen, N. M. AlYami, D. H. Anjum and O. M. Bakr, Effect of Precursor Ligands and Oxidation State in the Synthesis of Bimetallic Nano-Alloys, *Chem. Mater.*, 2015, **27**, 4134–4141.
- 42 C. Zhang, W. Sandorf and Z. Peng, Octahedral Pt₂CuNi Uniform Alloy Nanoparticle Catalyst with High Activity and Promising Stability for Oxygen Reduction Reaction, *ACS Catal.*, 2015, **5**, 2296–2300.
- 43 J. Mao, *et al.* Seed-mediated synthesis of hexameric octahedral PtPdCu nanocrystals with high electrocatalytic performance, *Chem. Commun.*, 2015, **51**, 15406–15409.
- 44 A. Kovács, R. Schierholz and K. Tillmann, FEI Titan G2 80-200 CREWLEY, *Journal of Large-Scale Research Facilities*, 2016, **2**, A43.
- 45 L. L. Wang and D. D. Johnson, Predicted trends of core-shell preferences for 132 late transition-metal binary-alloy nanoparticles, *J. Am. Chem. Soc.*, 2009, **131**, 14023–14029.
- 46 N. Cedex, Copper(II) complexation kinetics with hydroxyoximes in CTAB micelles Effect of extractant hydrophobicity and additives, *J. Chem. Soc., Faraday Trans.*, 1996, **92**, 249–255.
- 47 S. H. Wu and D. H. Chen, Synthesis of high-concentration Cu nanoparticles in aqueous CTAB solutions, *J. Colloid Interface Sci.*, 2004, **273**, 165–169.
- 48 D. Yoon, *et al.* One pot synthesis of hollow Cu-doped Ru octahedral nanocages via an in situ generated metastable Cu nanoparticle template, *Nanoscale*, 2014, **6**, 12397–12402.
- 49 B. Y. Xia, W. T. Ng, H. B. Wu, X. Wang and X. W. Lou, Self-supported interconnected Pt nanoassemblies as highly stable electrocatalysts for low-temperature fuel cells, *Angew. Chem., Int. Ed.*, 2012, **51**, 7213–7216.
- 50 X. Huang, L. Cao, Y. Chen, E. Zhu, Z. Lin, M. Li and T. Mueller, *et al.* High-performance transition metal - doped Pt₃Ni octahedra for oxygen reduction reaction, *Science*, 2015, **348**, 1230–1234.
- 51 C. Chen, *et al.* Highly crystalline multimetallic nanoframes with three-dimensional electrocatalytic surfaces, *Science*, 2014, **343**, 1339–1343.
- 52 F. Dionigi, *et al.* Controlling Near-Surface Ni Composition in Octahedral PtNi(Mo) Nanoparticles by Mo Doping for a Highly Active Oxygen Reduction Reaction Catalyst, *Nano Lett.*, 2019, **19**, 6876–6885.
- 53 C. Kim, *et al.* Alloy Nanocatalysts for the Electrochemical Oxygen Reduction (ORR) and the Direct Electrochemical Carbon Dioxide Reduction Reaction (CO₂RR), *Adv. Mater.*, 2019, **31**, 1–19.
- 54 A. Schlapka, M. Lischka, A. Groß, U. Käsberger and P. Jakob, Surface strain versus substrate interaction in heteroepitaxial metal layers: Pt on Ru(0001), *Phys. Rev. Lett.*, 2003, **91**, 016101.
- 55 Y. Shi, *et al.* Hollow PtCu nanorings with high performance for the methanol oxidation reaction and their enhanced durability by using trace Ir, *J. Mater. Chem. A*, 2020, **8**, 3795–3802.
- 56 N. M. Marković, B. N. Grgur, C. A. Lucas and P. N. Ross, Electrooxidation of CO and H₂/CO mixtures on Pt(111) in acid solutions, *J. Phys. Chem. B*, 1999, **103**, 487–495.
- 57 A. López-Cudero, A. Cuesta and C. Gutiérrez, Potential dependence of the saturation CO coverage of Pt electrodes: The origin of the pre-peak in CO-stripping voltammograms. Part 1: Pt(1 1 1), *J. Electroanal. Chem.*, 2005, **579**, 1–12.
- 58 M. K. Debe, Electrocatalyst approaches and challenges for automotive fuel cells, *Nature*, 2012, **486**, 43–51.

- 59 H. A. Gasteiger and N. M. Markovic, Just a Dream—or Future Reality?, *Science*, 2009, **324**, 1029–1031.
- 60 F. J. Vidal-Iglesias, R. M. Arán-Ais, J. Solla-Gullón, E. Herrero and J. M. Feliu, Electrochemical characterization of shape-controlled Pt nanoparticles in different supporting electrolytes, *ACS Catal.*, 2012, **2**, 901–910.
- 61 P. Urchaga, S. Baranton, C. Coutanceau and G. Jerkiewicz, Electro-oxidation of CO chem on Pt nanosurfaces: Solution of the peak multiplicity puzzle, *Langmuir*, 2012, **28**, 3658–3663.
- 62 M. Watanabe and S. Motoo, Electrocatalysis by ad-atoms. Part II. Enhancement of the oxidation of methanol on platinum by ruthenium ad-atoms, *J. Electroanal. Chem. Interfacial Electrochem.*, 1975, **60**, 267–273.
- 63 J. Lan, C. Li, T. Liu and Q. Yuan, One-step synthesis of porous PtNiCu trimetallic nanoalloy with enhanced electrocatalytic performance toward methanol oxidation, *J. Saudi Chem. Soc.*, 2019, **23**, 43–51.
- 64 A. Glösen, *et al.* Dealloyed PtNi-Core-Shell Nanocatalysts Enable Significant Lowering of Pt Electrode Content in Direct Methanol Fuel Cells, *ACS Catal.*, 2019, **9**, 3764–3772.